Implementation of Transition Modeling for Analysis and Optimization of Two-Dimensional Airfoil Problems

Zhi Yang [*] Dimitri J. Mavriplis [†]

Department of Mechanical Engineering, University of Wyoming, Laramie, WY 82071

This paper describes the implementation of various transition models used in conjunction with a single-equation turbulence model for predicting transitional flow over single and multiple element airfoil configurations. The analysis problem is formulated as well as the corresponding adjoint problem of the fully coupled flow-turbulence-transition equations. Test problems are shown for the computation of transitional airfoil cases, and the design optimization of a transitional airfoil using the adjoint-derived sensitivities is also demonstrated.

I. Introduction

Environmental responsibility and economic considerations require the aviation industry to develop more efficient transport aircraft with less fuel burn, emissions and noise. Drag reduction is a significant issue in aircraft design. Less drag means less fuel consumption, hence lower emissions. With increasing computational capability, CFD has become a powerful tool for aerodynamic analysis and design. It has been common in the context of aerodynamic shape optimization that the flows be considered as fully turbulent. In high-Reynolds number applications, the fully turbulent assumption is quite reasonable, because the flows usually transitions very close to the leading edge of the wing. However, for a large number of applications with lower Reynolds numbers, where the dominant feature in the flow field is laminar-turbulent transition, the fully turbulent assumption becomes questionable. Moreover, recent research has shown that the benefits of the natural laminar flow(NLF) is a key element in achieving significant drag reduction. The ability to accurately predict transition in RANS calculations and to incorporate laminar-turbulent transition calculations into the shape optimization process therefore takes on additional importance.

The turbulence models used in Reynolds-Averaged Navier-Stokes solvers usually cannot predict the transition locations in a flowfield. To predict transition, one must apply a transition criterion. Accurately, reliably and automatically predicting laminar-turbulent transition continues to be a challenge in CFD. In recent years, many researchers have investigated different approaches to incorporate transition prediction into RANS solvers. One approach is to solve additional locally defined transport equations, for example the local-correlation transition model, originally proposed by Menter et al.[15] and more fully developed by Langtry and Menter.[7] The model of Langtry and Menter solves for two additional transported scalars: intermittency γ, which defines whether the flow is laminar or turbulent, and a transitional momentum-thickness Reynolds number Re_θ, which controls the transition correlations. More recently, Menter et al.[16] presented a one-equation model by replacing the Re_θ equation with algebraic relations, thus simplifying the correlations for the transition onset prediction. Menter's γ-Re_θ transition model is designed to be coupled with the $k-\omega$ SST turbulence model. Medida and Baeder[14] modified and coupled Menter's γ-Re_θ original transition model with the one-equation Spalart-Allmaras(SA) turbulence model.[20] Another approach for transition modeling can be found in the amplification factor transport (AFT) model of Coder and Maughmer.[3] The AFT model is based on e^N theory, specifically the approximate envelope method of Drela and Giles.[5] AFT has been coupled with both the SA and SST turbulence models. The lack of general Galilean invariance in the AFT model has been fixed in a recent paper.[2] Coder's 2014 and 2017 AFT models are one equation transition models. Coder[4] presented an enhanced two-equation AFT transition model by adding a modified intermittency γ equation to the original amplification factor equation.

[*]Research Scientist, AIAA member; email: zyang@uwyo.edu

[†]Professor, AIAA Associate Fellow; email: mavriplis@uwyo.edu

Shape optimization methods are important tools in the aircraft design process. Many shape optimization techniques for aircraft have been demonstrated in previous research papers. Among several different kinds of optimization methods, gradient-based optimization has been used in many cases for aircraft design. In particular, the evaluation of aircraft performance objectives such as lift and drag requires significant computational effort due to the high cost of obtaining flow solutions, and thus gradient-based optimization is the only feasible method in many cases. Gradient-based optimization needs an efficient method for computing sensitivities of objective functions with respect to design variables. An adjoint method is well suited for computing sensitivities because the adjoint method can compute the gradients of all design variables at a computational cost that is independent of the number of design variables. Additionally, the discrete adjoint method employs direct differentiation of the discretized governing equations, thus obviating the need to assign an ambiguous perturbation value as required in the finite-difference method. Therefore, adjoint-based shape optimization represents a powerful technique for aircraft design optimization. Lee and Jameson[8] successfully coupled a RANS solver(Baldwin-Lomax turbulence model) to a boundary-layer code and an e^N database method for NLF design. The gradient calculations in their work did not include the transition prediction component. Khayatzadeh and Nadarajah[6] successfully incorporated the Langtry-Menter transport equation approach and $k-\omega$ SST turbulence model with an adjoint-based optimization framework in two dimensions and applied the framework to the design of low-Reynolds-number NLF airfoils. More recently, Rashad and Zingg[17] employed a RANS solver(Spalart-Allmaras turbulence model) and the e^N transition model to an adjoint-based optimization framework in two dimensions, and applied this approach to the design of natural-laminar-flow airfoils using single-point and multipoint optimizations.

In this paper, we investigate an e^N based transition model and the local-correlation transition model is coupled with the SA RANS solver under the adjoint-based optimization framework in two dimensions. In the following sections, we first outline the governing equations and the base flow solver, next the transition models used in this paper are presented, followed by the formulations of the adjoint-based optimization. Finally, some validation results are presented.

II. Governing Flow Field Equations

The Navier-Stokes equations in conservative form can be written as:

$$\frac{\partial \mathbf{U}}{\partial t} + \nabla \cdot (\mathbf{F}(\mathbf{U}) + \mathbf{G}(\mathbf{U})) = 0 \tag{1}$$

where $\mathbf{U}$ represents the vector of conserved quantities (mass, momentum, and energy), $\mathbf{F}(\mathbf{U})$ represents the convective fluxes and $\mathbf{G}(\mathbf{U})$ represents the viscous fluxes.

The Navier-Stokes equations are discretized by a central difference finite-volume scheme with additional matrix-based artificial dissipation on hybrid meshes which may include triangular and quadrilateral elements in two dimensions, or tetrahedra, pyramids, prisms and hexahedra in three dimensions. Second-order accuracy is achieved using a two-pass construction of the artificial dissipation operator, which corresponds to an undivided biharmonic operator. A single unifying edge-based data-structure is used in the flow solver for all types of elements. For multigrid calculations, a first-order accurate discretization is employed for the convective terms on coarse grid levels.[12,13] The turbulence model used in this paper is the one-equation Spalart-Allmaras(SA) turbulence model of the form:

$$\frac{D\tilde{\nu}}{Dt} = P_\nu - D_\nu + \frac{1}{\sigma}\left\{\frac{\partial}{\partial x_j}\left[(\nu+\tilde{\nu})\frac{\partial \tilde{\nu}}{\partial x_j}\right] + c_{b2}\frac{\partial \tilde{\nu}}{\partial x_j}\frac{\partial \tilde{\nu}}{\partial x_j}\right\} \tag{2}$$

where the production term is given as:

$$P_\nu = c_{b1} S \tilde{\nu}(1 - f_{t2}) \tag{3}$$

and the destruction term is given as:

$$D_\nu = (c_{w1} f_w - \frac{c_{b1}}{\kappa^2} f_{t2})\left(\frac{\tilde{\nu}}{d}\right)^2 \tag{4}$$

III. Transition Model Formulation

The local flow variables available in the CFD code are used in the γ-$Re_{\theta t}$ correlation-based transition model to predict the laminar-turbulence transition. In this model, a transport equation for the turbulence

intermittency γ and another equation for the transport of the momentum-thickness Reynolds number $Re_{\theta t}$ are solved. The intermittency equation is given as:

$$\frac{D\rho\gamma}{Dt} = P_\gamma - D_\gamma + \frac{\partial}{\partial x_j}\left[\left(\mu + \frac{\mu_t}{\sigma_f}\right)\frac{\partial\gamma}{\partial x_j}\right] \tag{5}$$

where the production term is

$$P_\gamma = F_{length} C_{a1} \rho S [\gamma F_{onset}]^{0.5} (1 - C_{e1}\gamma) \tag{6}$$

and the destruction term is

$$D_\gamma = C_{a2}\rho\Omega\gamma F_{turb}(C_{e2}\gamma - 1) \tag{7}$$

and the momentum-thickness Reynolds number transport equation is given as:

$$\frac{D\rho\tilde{Re_{\theta t}}}{Dt} = c_{\theta t}\frac{(\rho U)^2}{500\mu}(Re_{\theta t} - \tilde{Re_{\theta t}})(1 - F_{\theta t})\frac{\partial}{\partial x_j}\left[\sigma_{\theta t}(\mu + \mu_t)\frac{\partial\tilde{Re_{\theta t}}}{\partial x_j}\right] \tag{8}$$

The γ-$Re_{\theta t}$ transition model is designed to be coupled with the $k-\omega$ SST turbulent model by Menter al et.[7,15] Later the γ-$Re_{\theta t}$ transition model was modified and extended to be coupled with the SA turbulence model by Medida and Baeder.[14] The solution of the intermittency transport equation is used to control the production and destruction terms of the original SA turbulence model. The function f_{t2} is set to zero and the production and destruction terms in the SA turbulence model become:

$$\tilde{P_\nu} = \gamma P_\nu \quad and \quad \tilde{D_\nu} = min(max(\gamma, \beta), 1.0)D_\nu, \quad \beta = 0.5 \tag{9}$$

Details of the terms of the γ-$Re_{\theta t}$ transition model and the boundary conditions can be found in Menter's paper[7,15] and Medida's paper.[14]

The AFT model[3] presented by Coder and Maughmer predicts the development of the instability envelope amplification factor, $\tilde{n}$, through the solution of an advection-diffusion equation,

$$\frac{D\tilde{n}}{Dt} = \rho\Omega F_{crit} F_{growth}\frac{\partial\tilde{n}}{\partial Re_\theta} + \frac{\partial}{\partial x_j}\left[(\mu + \sigma_n\mu_t)\frac{\partial\tilde{n}}{\partial x_j}\right] \tag{10}$$

The source term in above equation is based on the integral boundary-layer shape factor, H_{12}, which is estimated using a localized shape factor H_L to maintain compatibility with CFD solvers. The original formulation of H_L proposed in reference[3] is not Galilean invariant. Following the work of Menter et al.,[16] Coder[2] proposed a new local shape factor:

$$H_L = \frac{d^2}{\mu}[\nabla(\rho\vec{u}\cdot\nabla d)\cdot\nabla d] \tag{11}$$

This shape factor is entirely localized and has no dependence on the free-stream conditions, nor any assumptions about the outer flow behavior. Galilean invariance is attained through the use of the wall distance as the length scale and the use of the wall-normal direction for evaluating the velocity derivative.

The interaction of the amplification-factor-transport model and the SA turbulence model is obtained by modifying the function f_{t2} in the production and destruction terms in the original SA turbulence model:

$$f_{t2} = c_{t3}\{1 - \exp[2(\tilde{n} - N_{crit})]\}\exp\left[-c_{t4}\left(\frac{\tilde{\nu}}{\nu}\right)^2\right] \tag{12}$$

An improved AFT model was recently proposed by Coder[4] by adding another transport equation for the intermittency γ:

$$\frac{D\tilde{\gamma}}{Dt} = c_1\rho S F_{onset}[1 - \exp(\tilde{\gamma})] - c_2\rho\Omega F_{turb}[c_3\exp(\tilde{\gamma}) - 1] + \frac{\partial}{\partial x_j}\left[(\mu + \sigma_\gamma\mu_t)\frac{\partial\tilde{\gamma}}{\partial x_j}\right] \tag{13}$$

The new AFT2017b(AFT2) model is coupled with the original SA turbulence model by modifying the f_{t2} function:

$$f_{t2} = c_{t3}[1 - \exp(\tilde{\gamma})] \tag{14}$$

The details of the terms of the AFT2 transition model and the boundary conditions can be found in Coder's paper.[2–4]

IV. Adjoint-Based Optimization Procedure

In general, the shape design optimization process consists of at least four sequential steps. Assuming an existing geometry and computational mesh already exist, and the design variables and objective functions are specified, the initial step consists of using the design variables to define a new deformed surface mesh geometry, producing specific values for the coordinates of the surface mesh. The surface mesh coordinates are then used to compute the values of the interior mesh coordinates, usually through a mesh deformation technique which aims to provide a smooth interior mesh with no overlapping cells. The third step involves the computation of the flow field on this new deformed mesh, and the fourth (final) step involves the computation of the objective function using the newly computed flow field. The design optimization problem can be written as:

$$L(\mathbf{D}) = L(F_3(F_2(F_1((D))) \tag{15}$$

with

$$\mathbf{x}_{surf} = F_1(\mathbf{D}) \tag{16}$$

$$\mathbf{x}_{int} = F_2(\mathbf{x}_{surf}) \tag{17}$$

$$\mathbf{w} = F_3(\mathbf{x}_{int}) \tag{18}$$

$$L = L(\mathbf{w}, \mathbf{x}_{int}) \tag{19}$$

where $\mathbf{D}$ and L represent the design variables and objective, $\mathbf{x}_{surf}$ represents the surface grid point coordinates, $\mathbf{x}_{int}$ represents the interior grid point coordinates, and $\mathbf{w}$ represents the flow, turbulence and transition variables on the deformed grid. A straight forward differentiation of equation (15) leads to the following expression for the sensitivity derivatives:

$$\frac{dL}{d\mathbf{D}} = \frac{\partial L}{\partial \mathbf{w}} \cdot \frac{\partial \mathbf{w}}{\partial \mathbf{x}_{int}} \cdot \frac{\partial \mathbf{x}_{int}}{\partial \mathbf{x}_{surf}} \cdot \frac{\partial \mathbf{x}_{surf}}{\partial \mathbf{D}} + \frac{\partial L}{\partial \mathbf{x}_{int}} \cdot \frac{\partial \mathbf{x}_{int}}{\partial \mathbf{x}_{surf}} \cdot \frac{\partial \mathbf{x}_{surf}}{\partial \mathbf{D}} \tag{20}$$

The $\frac{\partial \mathbf{x}_{surf}}{\partial \mathbf{D}}$ term represents the sensitivity of the surface mesh with respect to the design variables. The $\frac{\partial \mathbf{x}_{int}}{\partial \mathbf{x}_{surf}}$ term represents the sensitivity of the interior mesh point positions with respect to surface point displacements. Usually, the interior mesh displacements are computed by solving the equation:

$$[K]\delta\mathbf{x}_{int} = \delta\mathbf{x}_{surf} \tag{21}$$

where $[K]$ represents the stiffness matrix of the mesh motion equations. Then the sensitivities can be written as:

$$\frac{\partial \mathbf{x}_{int}}{\partial \mathbf{x}_{surf}} = [K]^{-1} \tag{22}$$

The term $\frac{\partial \mathbf{w}}{\partial \mathbf{x}_{int}}$ can be obtained by linearization about the converged state $\mathbf{R}(\mathbf{w}(\mathbf{x}_{int}), \mathbf{x}_{int}) = 0$ in the following relation:

$$\left[\frac{\partial \mathbf{R}}{\partial \mathbf{w}}\right] \frac{\partial \mathbf{w}}{\partial \mathbf{x}_{int}} = -\frac{\partial \mathbf{R}}{\partial \mathbf{x}_{int}} \tag{23}$$

or re-written as:

$$\frac{\partial \mathbf{w}}{\partial \mathbf{x}_{int}} = -\left[\frac{\partial \mathbf{R}}{\partial \mathbf{w}}\right]^{-1} \frac{\partial \mathbf{R}}{\partial \mathbf{x}_{int}} \tag{24}$$

Substituting the above expressions into equation (20) leads to:

$$\frac{dL}{d\mathbf{D}} = -\frac{\partial L}{\partial \mathbf{w}} \cdot \left[\frac{\partial \mathbf{R}}{\partial \mathbf{w}}\right]^{-1} \frac{\partial \mathbf{R}}{\partial \mathbf{x}_{int}} [K]^{-1} \frac{\partial \mathbf{x}_{surf}}{\partial \mathbf{D}} + \frac{\partial L}{\partial \mathbf{x}_{int}} \cdot [K]^{-1} \frac{\partial \mathbf{x}_{surf}}{\partial \mathbf{D}} \tag{25}$$

The adjoint model is obtained by transposing above equation:

$$\frac{dL}{d\mathbf{D}}^T = \frac{\partial \mathbf{x}_{surf}}{\partial \mathbf{D}}^T [K]^{-T} \left[\frac{\partial L}{\partial \mathbf{x}_{int}}^T - \frac{\partial \mathbf{R}}{\partial \mathbf{x}_{int}}^T \left[\frac{\partial \mathbf{R}}{\partial \mathbf{w}}\right]^{-T} \frac{\partial L}{\partial \mathbf{w}}^T\right] \tag{26}$$

For a single objective function, the adjoint model consists of the following steps:

1. Obtain objective flow sensitivity vector $\frac{\partial L}{\partial \mathbf{w}}$

2. Iteratively solve the adjoint flow problem:

$$\left[\frac{\partial \mathbf{R}}{\partial \mathbf{w}}\right]^T \Lambda_w = \frac{\partial L}{\partial \mathbf{w}}^T \qquad or \qquad \Lambda_w = \left[\frac{\partial \mathbf{R}}{\partial \mathbf{w}}\right]^{-T} \frac{\partial L}{\partial \mathbf{w}}^T \tag{27}$$

3. Obtain objective sensitivities with respect to interior mesh deformation

$$\frac{dL}{d\mathbf{x}^*_{int}}^T = \frac{\partial L}{\partial \mathbf{x}_{int}}^T - \frac{\partial \mathbf{R}}{\partial \mathbf{x}_{int}}^T \Lambda_w \tag{28}$$

4. Iteratively solve the adjoint mesh deformation problem:

$$[K]^T \Lambda_x = \frac{dL}{d\mathbf{x}^*_{int}}^T \qquad or \qquad \Lambda_x = [K]^{-T} \frac{dL}{d\mathbf{x}^*_{int}}^T \tag{29}$$

5. Compute final sensitivity:

$$\frac{dL}{d\mathbf{D}}^T = \frac{\partial \mathbf{x}_{surf}}{\partial \mathbf{D}}^T \Lambda_x \qquad or \qquad \frac{dL}{d\mathbf{D}} = \Lambda_x^T \frac{\partial \mathbf{x}_{surf}}{\partial \mathbf{D}} \tag{30}$$

We emphasize that in this formulation, the residual $\mathbf{R}$ represents the residual vector of all coupled equations, including flow, turbulence and transition. Therefore, the adjoint is based on the exact linearization of the fully coupled system $\left[\frac{\partial \mathbf{R}}{\partial \mathbf{w}}\right]$ which represents a block matrix with 7x7 blocks, consisting of 4 flow equations in 2D, one turbulence equation, and two transition equations. Although the steps described above appear to be relatively straight-forward, steps 2 and 4 in both cases require the solution of a set of field equations, while step 3 requires the evaluation of a complicated matrix-vector product. Furthermore, the term $\frac{\partial L}{\partial \mathbf{x}_{int}}$ must be constructed explicitly. Details of the techniques for implementing each of these steps effectively can be found in references.[9,10]

The addition of one or two transition equations often makes the fully coupled system of equations more difficult to converge fully. Obtaining deep convergence levels at each design step is important in order to obtain precise functional and sensitivity values for use in the optimization process. In order to obtain reliable convergence, we use a pseudo-transient continuation(PTC) Newton method[1] with added residual smoothing.[11]

There are many choices for the optimization algorithm in gradient-based optimization. The simplest one is the steepest-descent method. Although this method is easy to implement, it often exhibits poor performance when the number of design parameters is large. In the present work, LBFGS-B is used for the optimization algorithm. LBFGS-B[21] is a quasi-Newton method for bound-constrained optimization, which requires only sensitivity and objective function values. The LBFGS-B algorithm also can set the bounds of the design space to prevent invalid geometry configurations.

V. Validations and Results

A. Zero-Pressure-Gradient Flat Plate

A flat plate with zero pressure gradient is the simplest boundary-layer flow. Its laminar-turbulent transition behavior has been widely studied for a range of freestream turbulence intensities. Figure 1a shows the mesh used in the flat plate case, which includes about 52,000 nodes with normal spacing at the wall of 4×10^{-6} and 255 points on the wall. Predicted skin-friction distributions obtained by the λ-$Re_{\theta t}$ model and the AFT model coupled with the SA turbulence model are plotted in Figure 1b with experiment data, and the Blasius laminar profile. The figure shows good agreement between predicted results and experiment data for different freestream turbulence levels. The N factor contours are shown in Figure 1c.

B. NASA NLF-0416 Airfoil

The NASA NLF-0416 was designed for general aviation applications and was tested in the Low-Turbulence Pressure Tunnel (LTPT) at NASA Langley. The near field mesh for the NLF-0416 airfoil is shown in Figure 2a, which includes approximately 63,000 nodes with normal wall spacing of 1.2×10^{-6} chord lengths and 775 points on the airfoil surface. The resulting drag polars for $Re = 4.0 \times 10^6$ are plotted in Figure 2b.

The agreement between the transitional predictions and the LTPT data are good for both the λ-$Re_{\theta t}$ model and the AFT2 model. Figure 2c and 2d show the comparison of the skin-friction distributions at $\alpha = 0^\circ$ and $\alpha = -2^\circ$, respectively.

C. S204, slotted Natural-Laminar-Flow Airfoil

The S204 airfoil[19] is a slotted natural-laminar-flow (SNLF) airfoil for light business jet applications. The S204 is a two-element configuration designed to achieve higher lift coefficients and lower drag coefficients than the single-element natural-laminar-flow airfoils. The S204 airfoil is designed in such a way to keep the fore element entirely laminar in order to reduce overall drag. The SNLF concept as well as the S204 configuration is proprietary to Airfoils Inc. and protected by a patent, requiring a license for its use. The specific airfoil geometry used in this paper was obtained by digitizing a figure of the airfoil geometry in reference[19] with permission from the author. Because the performance of SNLF airfoils can be sensitive to small geometry perturbations, this approach may not be entirely accurate due to the approximate airfoil coordinates used in this case. Figure 3a shows the near field mesh for the S204 airfoil. The normal wall spacing in this mesh is 1.2×10^{-6} chord lengths. There are 390 surface mesh points on the main element and 226 points on the slat. The total number of mesh points is about 51,000. The drag polars for $M = 0.5$, $Re = 12 \times 10^6$ and freestream turbulence intensity $Tu_\infty = 0.07\%$ are plotted in Figure 3b. The agreement between the transitional predictions and the reference results[19] is generally good. Figure 3c shows the pressure coefficient distribution at $\alpha = 0^\circ$. The skin-friction distribution at $\alpha = 0^\circ$ is shown in Figure 3d, which shows entirely laminar flow on the fore element upper surface.

D. MD 30P/30N Multi-element Airfoil

The McDonnell-Douglas 30P/30N airfoil is a conventional multi-element high-lift configuration that was tested in the NASA Langley Low-Turbulence Pressure Tunnel(LTPT) in 1990s. The unforced transition tests on all elements at different Reynolds numbers and angles of attack were conducted in the LTPT. The measured transition locations[18] are given as a range in terms of x/c, and are available for angles of attack of 4° , 8° , 19° , and 21°. The MD 30P/30N configuration is a good candidate for two-dimensional code validation. Figure 4 shows the near field mesh for the MD 30P/30N configuration. There are 69,000 nodes in this mesh with a normal wall spacing of 1.2×10^{-6} chord lengths. The number of mesh points on the main element, the slat and the flap are 275, 302 and 215, respectively. Figures 5 show the intermittency at $\alpha = 19^\circ$. Figures 6 show the comparison of the skin-friction distributions at $\alpha = 19^\circ$ on the slat, main element and flap between fully turbulent (SA alone) and transitional calculations using the AFT2 model. The transition locations predicted by the AFT2 model qualitatively agree with the reported ranges on the slat and main element as shown in Table 1. The disagreement on the flap is thought to be due to the relatively coarse mesh resolution present in the main cove region, as seen in Figure 4 and deserves further consideration.

Table 1. Comparison of measured and predicted transition positions.

	$\alpha = 19^\circ$	
	Experiment[18]	Predicted Results
Slat Upper (x/c)	$[-0.085, -0.082]$	$[-0.084, -0.08]$
Main Upper (x/c)	$[0.061, 0.068]$	$[0.06, 0.08]$
Flap Upper (x/c)	$[0.892, 0.921]$	Fully turbulent

E. Optimization NACA0012

In order to demonstrate the current adjoint-based optimization capability, a NACA0012 airfoil in viscous flow with free transition is optimized for reducing drag or maximizing the ratio of lift over drag. In this case the AFT2 transition model is used with the Spalart-Allmaras turbulence model. The flow conditions include a freestream $M = 0.2$, an angle of attack of $\alpha = 2.31^\circ$ and $Re = 2 \times 10^6$. The near field mesh for the NACA0012 airfoil is shown in Figure 7a. Figure 7b shows a typical convergence history for both the flow variables and the turbulence/transition variables. In this case we use a Newton-Krylov method with

pseudo-transient continuation augmented with a residual smoothing technique[11] for ensuring convergence of all equations to machine zero. The ability to converge each design point throughout the optimization to very low residual levels is important for success of the optimization process and the use of a Newton method has been found to be beneficial in this context. The objective L for minimizing drag at prescribed lift is constructed as:

$$L = (C_L - C_{L_{target}})^2 + 10C_D^2 \tag{31}$$

Figure 8a shows the comparison between the initial and final optimized airfoil shape. Bezier parameterizations are used in this case, with 12 design variables used to optimize the airfoil shape. Figure 8b show the convergence of the objective function, the lift coefficient and the drag coefficient versus design cycles. The comparison of the surface pressure coefficient and the skin-friction distributions are shown in the Figure 9a and Figure 9b, respectively. Overall, the drag is reduced by 13 counts in 16 design cycles in this optimization.

The objective L for maximizing the ratio of lift and drag is constructed as:

$$L = \left| \frac{C_D}{C_L} \right| \tag{32}$$

Similarly to the previous optimization case, Bezier parameterizations with 12 design variables are used. Figure 10a shows the airfoil shape comparison while Figure 10b shows the convergence of the objective function, the lift coefficient and the drag coefficient versus design cycles. The comparison of the surface pressure coefficient and the skin-friction distribution are shown in the Figure 11a and Figure 11b, respectively. Table 2 summarizes the comparison of the drag reduction and the lift-drag ratio for the baseline airfoil and optimized airfoils. Overall, the lift to drag ratio is increased from 23.8 to 46.7 in 14 design cycles for this case.

Table 2. Comparison of lift and drag coefficients for the NACA0012 and the optimized airfoil.

	C_L	C_D	$\Delta(C_D)$	$\frac{C_L}{C_D}$
Baseline	0.2402	0.01011	-	23.8
Optimized for $\min_{C_{L_{target}}} (C_D)$	0.2393	0.00882	-0.00129	-
Optimized for $\max(\frac{C_L}{C_D})$	0.4764	0.01021	-	46.7

VI. Conclusion

The incorporation of current state-of-the-art transition models has been described and demonstrated in this work. The performance of two predictive transition models coupled with the Spalart-Allamaras single-equation turbulence model for two-dimensional single and multi-element airfoil configurations has been examined through a series of computational test cases. The fully coupled adjoint of the flow-turbulence-transition system of equations has also been derived and demonstrated for use in an airfoil optimization test case. These results indicate that current transition models can be used for predictive aerodynamic airfoil problems as well as for design optimization of airfoil performance.

VII. Acknowledgments

This work was supported by NASA University Led Initiative (ULI) grant NNX17AJ95A entitled "Advanced Aerodynamic Design Center for Ultra-Efficient Commercial Vehicles" under a subcontract from the University of Tennessee at Knoxville.

References

[1]M. Ceze and K. J. Fidkowski. Constrained pseudo-transient continuation. *International Journal for Numerical Methods in Engineering*, 102:1683–1703, Mar. 2015.

[2]J. G. Coder. Enhancement of the amplification factor transport transition modeling framework. AIAA Paper 2017-1709, 55th AIAA Aerospace Sciences Meeting, January, 2017.

[3]J. G. Coder and M. D. Maughmer. Computational fluid dynamics compatible transition modeling using an amplification factor transport equation. *AIAA Journal*, 52(11):2506–2512, 2014.

[4]J. G. Coder, T. H. Pulliam, and J. C. Jensen. Contributions to HiLiftPW-3 using structured, overset grid methods. AIAA Paper 2018-1039, AIAA SciTech Forum, January, 2018.

[5]M. Drela and M. B. Giles. Viscous-inviscid analysis of transonic and low-Reynolds number airfoils. *AIAA Journal*, 25(10):1347–1355, 1987.

[6]P. Khayatzadeh and S. K. Nadarajah. Aerodynamic shape optimization of natural laminar flow (NLF) airfoils. AIAA Paper 2012-0061, 50th AIAA Aerospace Sciences Meeting and Exhibit, January, 2012.

[7]R. B. Langtry and F. R. Menter. Correlation-based transition modeling for unstructured parallelized computational fluid dynamics codes. *AIAA Journal*, 47(12):2984–2906, 2009.

[8]J. Lee and A. Jameson. Natural-laminar-flow airfoil and wing design by adjoint method and automatic transition prediction. AIAA Paper 2009-0897, 47th AIAA Aerospace Sciences Meeting and Exhibit, January, 2009.

[9]D. J. Mavriplis. Formulation and multigrid solution of the discrete adjoint for optimization problems on unstructured meshes. AIAA Paper 2005-0319, AIAA Aerospace Sciences Meeting, Reno, NV, January, 2005.

[10]D. J. Mavriplis. A discrete adjoint-based approach for optimization problems on three-dimensional unstructured meshes. AIAA Paper 2006-0050, AIAA Aerospace Sciences Meeting, Reno, NV, January, 2006.

[11]D. J. Mavriplis, B. Ahrabi, and M. Brazell. Accelerating newton method continuation for CFD problems. AIAA Paper to be presented at Scitech 2019. San Diego CA, Jan. 2019.

[12]D. J. Mavriplis and S. Pirzadeh. Large-scale parallel unstructured mesh computations for 3D high-lift analysis. *AIAA Journal of Aircraft*, 36(6):987–998, Dec. 1999.

[13]D. J. Mavriplis and V. Venkatakrishnan. A unified multigrid solver for the Navier-Stokes equations on mixed element meshes. *International Journal of Computational Fluid Dynamics*, (8):247–263, 1997.

[14]S. Medida and J. D. Baeder. Application of the correlation-based γ-$Re_{\theta t}$ transition model to the Spalart-Allmaras turbulence model. AIAA Paper 2011-3979, 20th AIAA Computational Fluid Dynamics Conference, June, 2011.

[15]F. R. Menter and R. L. and. S. Volker. Transition modelling for general purpose CFD codes. *Flow, Turbulence and Combustion*, 77:277–303, 2006.

[16]F. R. Menter, P. E. Smirnov, T. Liu, and R. Avancha. A one-equation local correlation-based transition model. *Flow, Turbulence and Combustion*, 95(4):583–619, 2015.

[17]R. Rashad and D. W. Zingg. Aerodynamic shape optimization for natural laminar flow using a discrete-adjoint approach. *AIAA Journal*, 54(11):3321–3337, 2016.

[18]C. L. Rumsey, T. B. Gatski, S. X. Ying, and A. Bertelrud. Prediction of high-lift flows using turbulent closure models. *AIAA Journal*, 36(5):765–777, 1998.

[19]D. M. Somers. Design of a slotted, natural-laminar-flow airfoil for business-jet applications. NASA/CRV2012-217559, July, 2012.

[20]P. R. Spalart and S. R. Allmaras. A one-equation turbulence model for aerodynamic flows. *La Recherche Aérospatiale*, 1:5–21, 1994.

[21]C. Zhu, R. H. Byrd, P. Lu, and J. Nocedal. LBFGS-B: A limited memory FORTRAN code for solving bound constrained optimization problems. Technical Report NAM-11, EECS Department, Northwestern University, 1994.

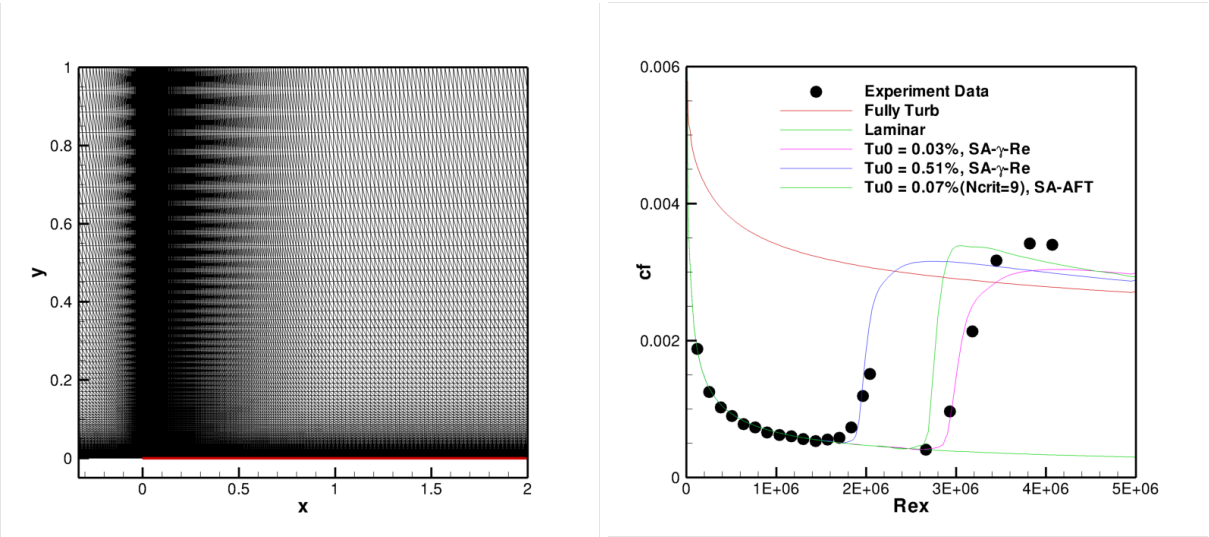

(a)

(b)

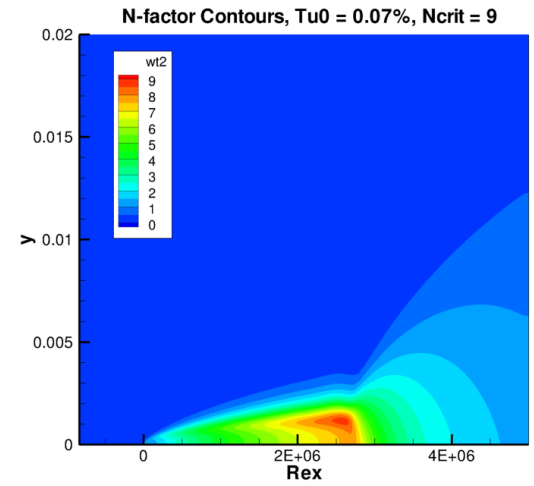

(c)

Figure 1. (a) Mesh for flat plate boundary layer test case (b) Cf comparison and (d) N factor contours with Ncrit=9

.

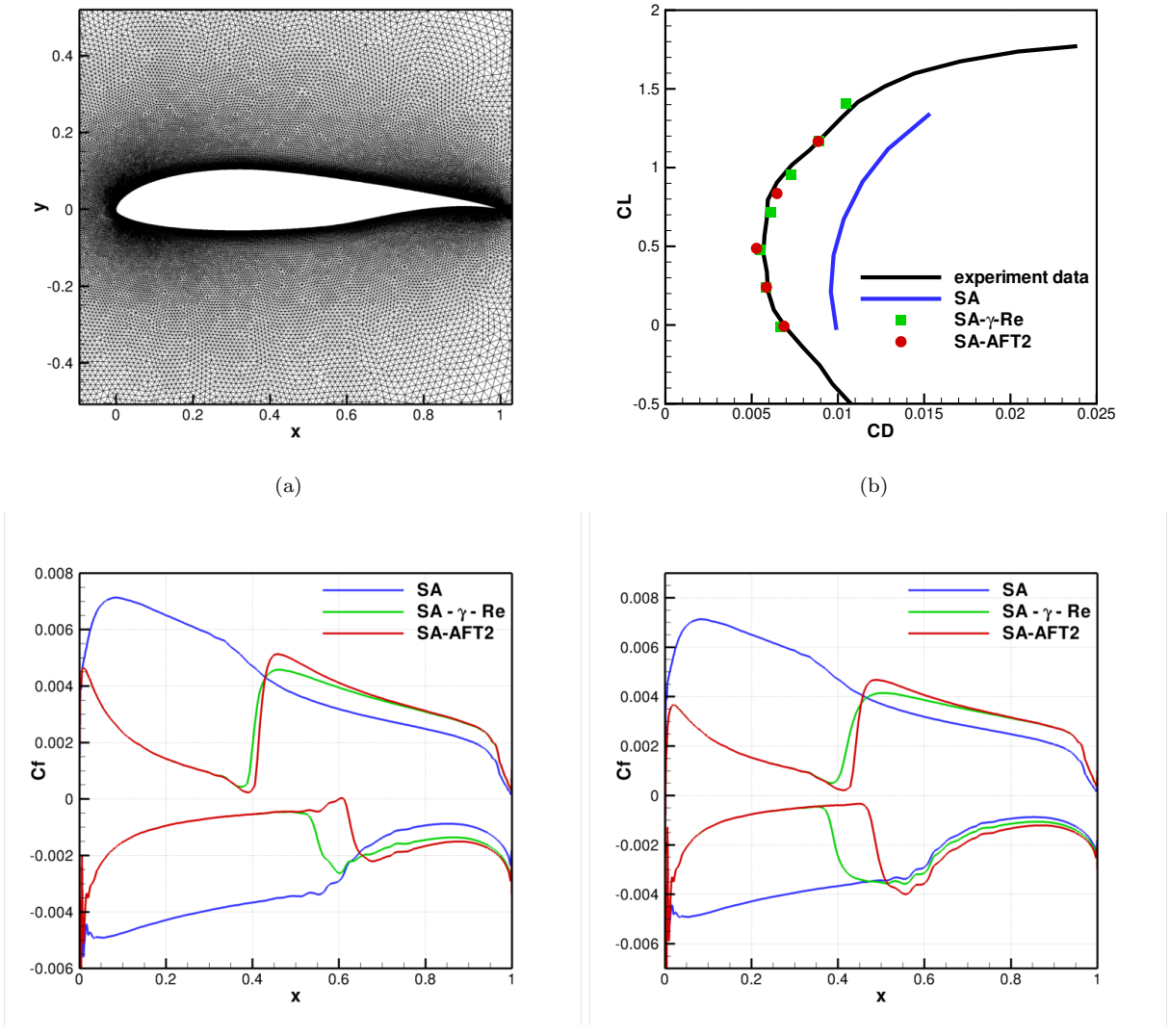

(a) (b)

(c) (d)

Figure 2. (a) Near field mesh for NLF0416 airfoil (b) Force comparison at $M = 0.2$, $Re = 4 \times 10^6$ and $Tu_\infty = 0.15\%$ (c) skin-friction distribution at $\alpha = 0^\circ$ and (d) skin-friction distribution at $\alpha = -2^\circ$

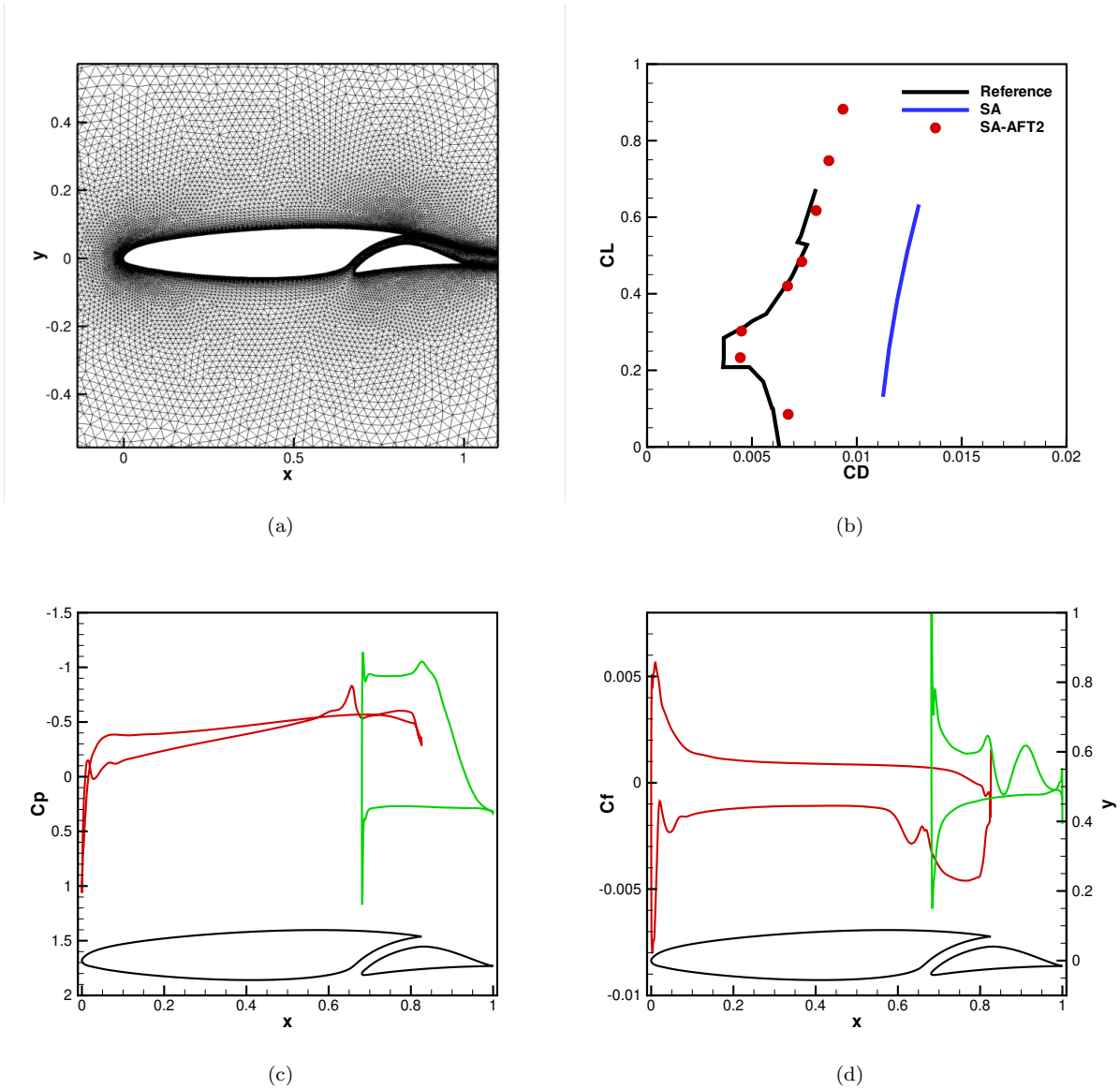

Figure 3. (a) Computational mesh for S204 slotted airfoil (b) force comparison at $M = 0.5$, $Re = 12 \times 10^6$ and $Tu_\infty = 0.07\%$ (c) pressure distribution (SA-AFT2) and (d) skin-friction distribution (SA-AFT2) at $\alpha = 0°$.

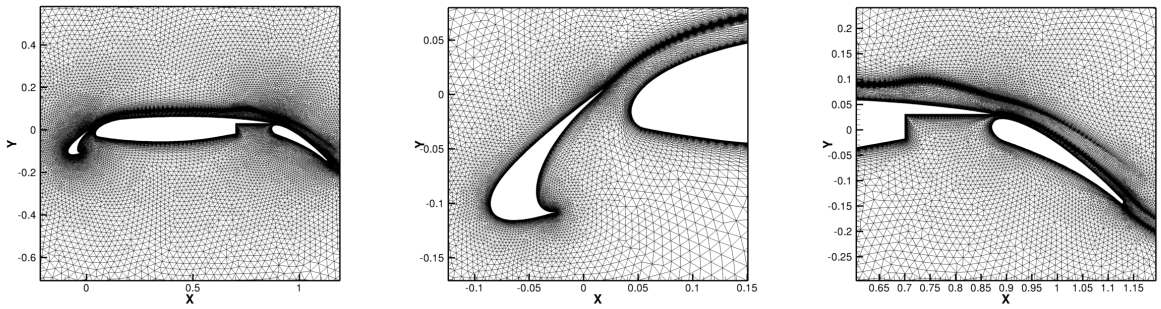

Figure 4. Near field mesh for MD-30P30N multi-element airfoil.

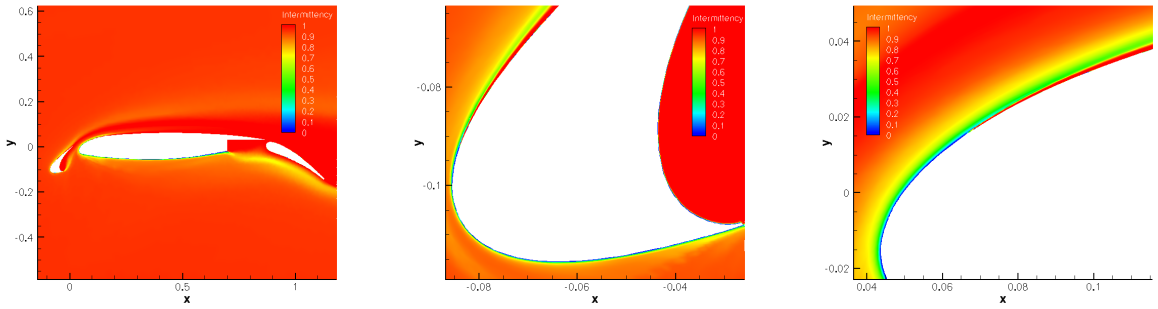

Figure 5. Intermittency contours at $\alpha = 19^\circ$ and $Re = 9 \times 10^6$, using SA-AFT2 transition model.

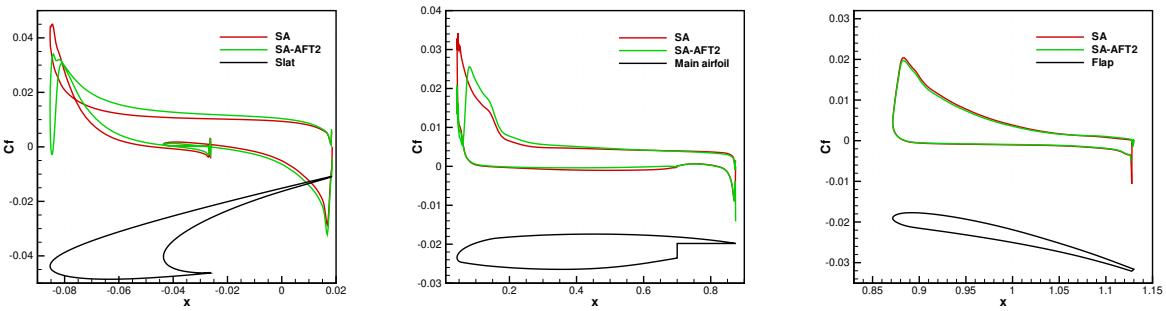

Figure 6. Computed skin-friction distribution on slat, main element and flap.

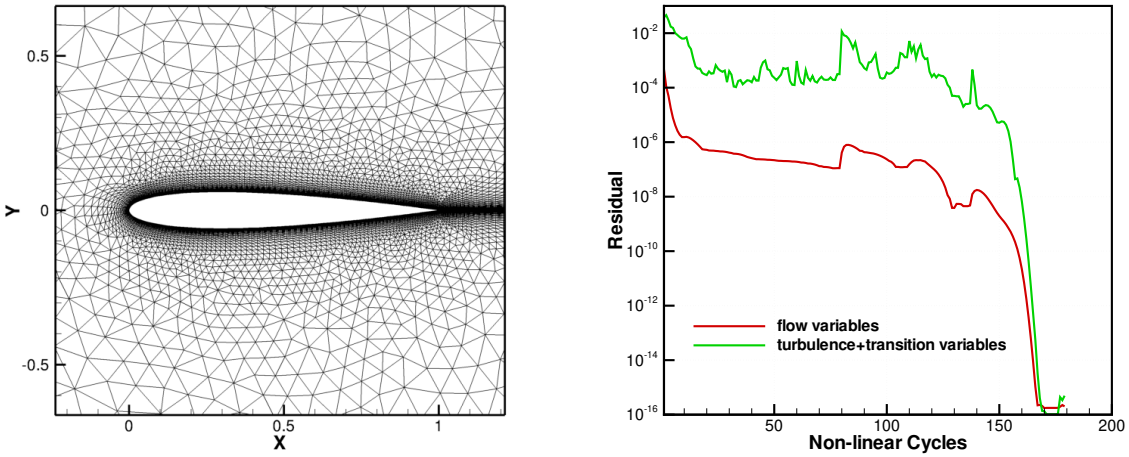

(a) (b)

Figure 7. (a) Near field computational mesh for NACA0012 airfoil (b) convergence history for flow variables and turbulence/transition variables.

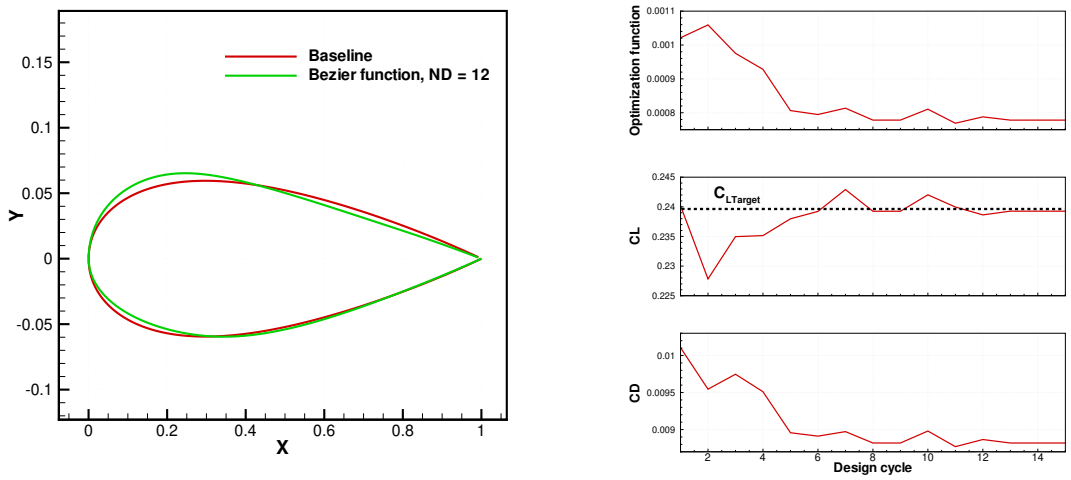

(a) (b)

Figure 8. Drag minimization at constant lift optimization problem: (a) NACA0012 airfoil shape comparison (b) Optimization function and forces vs. design cycles, SA-AFT2.

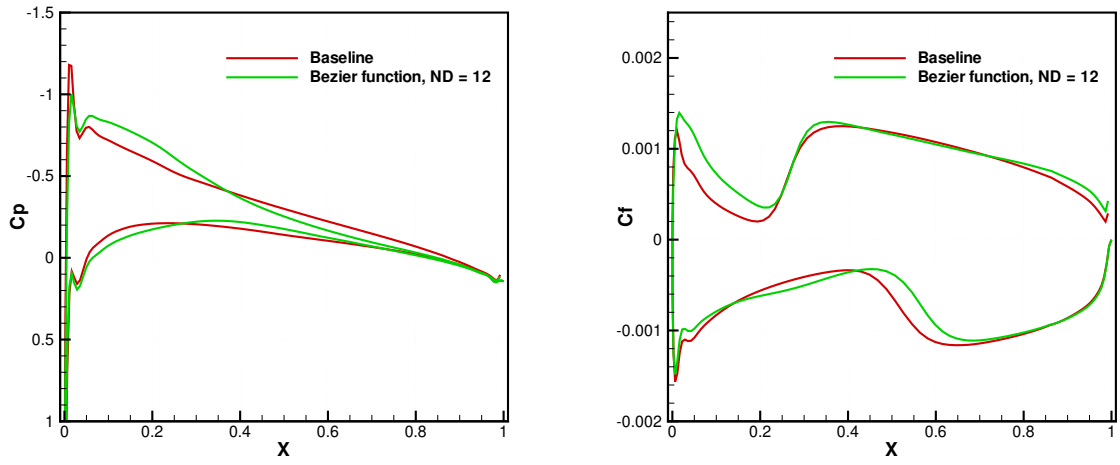

(a) (b)

Figure 9. Drag minimization at constant lift optimization problem:(a) Initial and optimized pressure distributions and (b) Initial and optimized skin-friction distributions, SA-AFT2

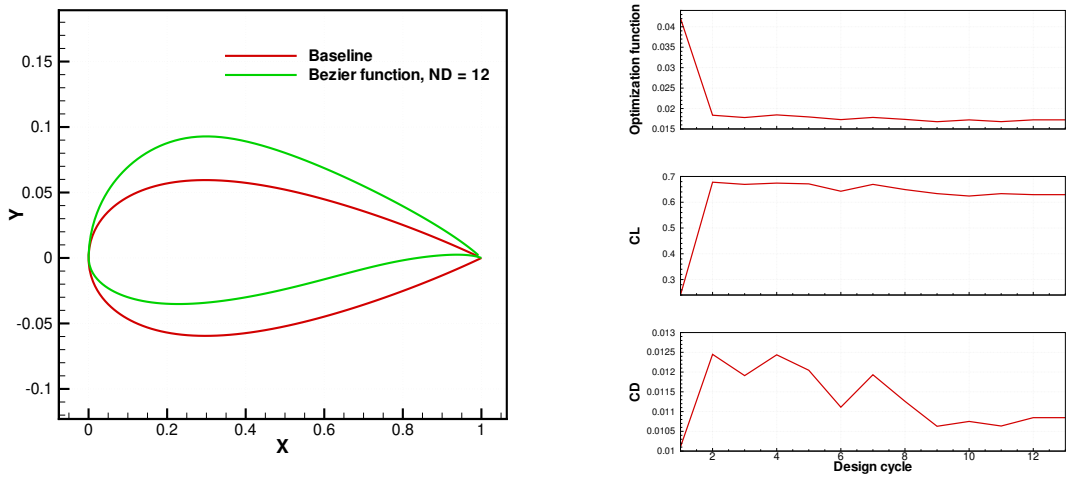

(a) (b)

Figure 10. Lift to drag ratio optimization problem: (a) NACA0012 airfoil shape comparison (b) Optimization function and forces vs. design cycles, SA-AFT2.

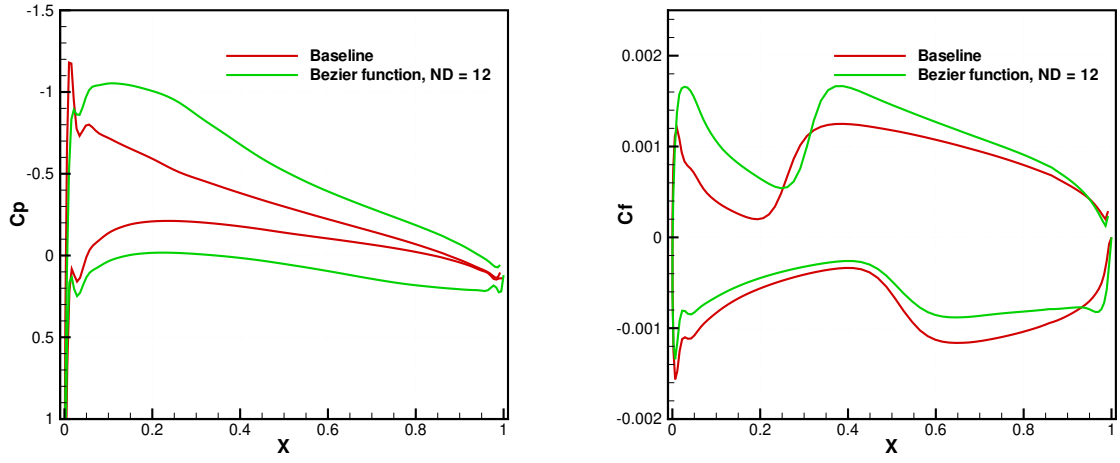

(a) (b)

Figure 11. Lift to drag ratio optimization problem:(a) Comparison of initial and optimized pressure distributions and (b) skin-friction distributions, SA-AFT2